RSC Advances

ROYAL SOCIETY OF CHEMISTRY

www.rsc.org/advances

A revisited phonon assignment and electro-mechanical properties of chromium disilicide

P. Hermet,* M. Khalil, R. Viennois, M. Beaudhuin,† D. Bourgogne, and D. Ravot

Institut Charles Gerhardt Montpellier,

UMR 5253 CNRS-UM2-ENSCM-UM1, Université Montpellier 2,

Place E. Bataillon, 34095 Montpellier Cédex 5, France

(Dated: January 14, 2015)

We report a complete study of the lattice dynamics, dielectric, elastic and piezolectric properties of the hexagonal semiconducting chromium disilicide ($CrSi_2$). From a combined experimental and theoretical study, we have revisited the phonon mode assignments at the zone-center, so that the contradictions met in previous experimental studies between 250 and 300 cm^{-1} are now explained and understood. We found that the temperature dependence of the Raman frequencies is mainly due to an implicit volume contribution and related to the large Gruneisen parameter. This explains why $CrSi_2$ has a moderate thermal conductivity although its Debye temperature is quite large. Optic and static dielectric constants have also been analyzed and discussed. The elastic constants of $CrSi_2$ are large, but this compound is quite brittle. In addition, the relatively low Poisson coefficient associated to the large negative Cauchy pressure of $CrSi_2$ indicate the angular nature of its bonding. The calculation of its piezoelectric coefficient shows a sizable value with a magnitude similar to that reported for α-quartz. This prediction requires, however, experimental confirmations.

Keywords: Phonons, First-principles, Raman, Infrared, Piezoelectric, $CrSi_2$

I. INTRODUCTION

Chromium disilicide ($CrSi_2$) is a p-type degenerate semiconductor with a narrow and indirect energy bandgap measured about 0.4 eV [1, 2]. It crystallizes in a hexagonal C40

*Electronic address: Patrick.Hermet@univ-montp2.fr(theory)

†Electronic address: Mickael.Beaudhuin@univ-montp2.fr(experiment)

structure within the $P6_222$ space group with Cr-atoms (resp. Si-atoms) in $3d$ (resp. $6j$) special Wyckoff position. This compound is interesting for high temperature applications due to its refractory properties, its relatively high melting point (1750 K), and its good resistance to oxidation [3]. Moreover, its high Seebeck coefficient (α) associated to its low electrical resistivity (ρ) make this compound promising for thermoelectric applications or even photoelectric source and detection in the near infrared region [1]. In addition, it is possible to obtain a high-quality strain-free epitaxial growth on Si (111) surfaces (mismatch of -0.14 %), which presents a strong interest in microelectronic [3].

$CrSi_2$ alloys have been intensively studied over the past 15 years, mainly for their thermoelectric (TE) properties. The TE potential of a material is evaluated by its reduced figure of merit: $ZT = \frac{\alpha^2 T}{\rho\kappa}$, where κ is the thermal conductivity. Thus, ZT has to be as high as possible. Pure $CrSi_2$ has a ZT$\approx$0.2 which is rather low with respect to the best TE materials based on silicon alloys (ZT$\approx$1 in the 600-900 K range) [4–8]. Recent papers have also shown the possibility to improve the power factor by alloying with Al, V, Mn, Fe, P, Ti [9–11]. However, $CrSi_2$ has a moderate thermal conductivity, $\kappa \approx$10 W.m^{-1}.K^{-1} at room temperature [7], which could be additionally reduced by adding defects or by controlling the nanostructure. In a previous work [11], we have shown that the combination of porosity and nanostructuration lead to decrease κ by a factor $\sim$10. This result is particularly interesting as it could lead to an increase of ZT. Unfortunately, this texturing also increases the electrical resistivity and is consequently not sufficiently beneficial to strongly improve its TE properties. In this context, the carefully study and understanding of the $CrSi_2$ phonon dynamics is fundamental to find the best way to scatter the phonons, and therefore increase ZT. Up to now, relatively few experimental information concerning the dynamical properties of $CrSi_2$ are available: Raman and infrared spectra were measured on bulk [12, 13] and thin films [2, 12, 14], but these spectra do not always agree and mode assignments remain difficult due to the lack of relevant theoretical support.

In this paper, we perform a complete study of the dynamical, dielectric, elastic and piezoelectric properties of $CrSi_2$ from first-principles based methods. Our study therefore covers all the linear couplings between applied static homogeneous electric field, strain, and periodic atomic displacements. Our theoretical results are compared to the experimental ones when available. The main objective of this work is the complete investigation of the microscopic physical properties of $CrSi_2$ for its potential industrial applications and more

notably for TE field. We also report theoretical infrared and Raman spectra, providing benchmark theoretical data directly useful for the assignments of experimental spectra and clarifying the previously proposed assignments.

This paper is organized as follows. The next section describes the experimental procedure to characterize the $CrSi_2$ sample and the detail of the Raman measurements. The theoretical framework of our calculations is given in Sec. III. Sec. IV is the heart of the article. First, the experimental study of the anharmonicity of the Raman lines shows that their temperature dependence is dominated by the volume contribution, leading to large Grüneisen parameter. The latter can also explain why $CrSi_2$ has a moderate thermal conductivity, although the calculation of its band structure gives a quite large Debye temperature (766 K). Then, we revisit the zone-center phonon assignments of $CrSi_2$ from a combined experimental and theoretical study, so that the contradictions met in the previous experimental studies concerning the vibration modes between 250 and 300 cm^{-1} are now explained and understood. Its static dielectric tensor is also discussed. Finally, we compute the piezoelectric coefficient of $CrSi_2$ and we predict a sizable value with a magnitude similar to that reported for α-quartz. This prediction needs, however, to be experimentally supported. Sec. V concludes the paper with the most important results of this work.

II. EXPERIMENTAL DETAILS

Polycrystalline samples were synthesized by arc melting of stoichiometric amount of high purity Cr (99.995%, Alfa Aesar) and Si lumps (99.999%, Alfa Aesar). Sample homogeneity is improved by re-melting the samples twice. X-ray diffraction experiments reveal that the $CrSi_2$ phase is almost pure. From Rietveld refinement, the lattice parameters were found to be: $a = 4.4317(3)$ Å and $c = 6.3655(2)$ Å in fair agreement with previous experimental data [3].

Temperature dependent micro-Raman experiments were measured on homogeneous sample areas with a Labram Aramis confocal microprobe analyzer (Horiba Jobin-Yvon) equipped with an Olympus microscope and a CCD cooled by a thermoelectric Peltier device. We used the 633 nm He-Ne laser line and a power of 0.7 mW. The resolution of the spectra was 1 cm^{-1}. For high temperature experiments, the samples were placed in a Microvision furnace HFS600Pb4. The counting time at the room temperature was twice longer than at higher

temperature. The resonant Raman effect was checked using the 531 nm Krypton ion laser line and a T64000 spectrometer (Horiba Jobin-Yvon). The latter is equipped with an Olympus microscope and a CCD cooled by nitrogen liquid. The resolution of the spectra was between 2 and 3 cm^{-1}. Special care was taken to avoid heating of the samples with too high laser power. This was especially true for the experiment with Krypton ion laser in which we have used power as low as 0.3 mW.

III. COMPUTATIONAL DETAILS

First-principles calculations are performed within the density functional theory (DFT) framework as implemented in the ABINIT package [15]. The exchange-correlation energy functional is evaluated using the local density approximation (LDA) parametrized by Perdew and Wang [16]. The all-electron potentials are replaced by norm-conserving pseudopotentials generated according to the Troullier-Martins scheme [17]. Cr($3d^5$, $4s^1$) and Si($3s^2$, $3p^2$)-electrons are considered as valence states. The electronic wave functions are expanded in plane-waves up to a kinetic energy cutoff of 55 Ha and integrals over the Brillouin zone are approximated by sums over a 8×8×8 mesh of special k-points according to the Monkhorst-Pack scheme [18]. Atomic relaxation are performed at the experimental lattice parameters (see previous section) until the maximum residual forces on each atom were less than 5.10^{-6} Ha/Bohr. This leads to an electronic band gap, E_g =0.49 eV, which is consistent with the experimental values [1, 2, 19] reported between 0.35 and 0.55 eV in the literature. Thus, the well-known DFT band-gap problem is less severe in $CrSi_2$ because the states on both sides of the band gap are mainly of $3d$-Cr character with only a small admixture of p and s states [13].

Dynamical matrix, dielectric constants, Born effective charges, elastic and piezoelectric constants are calculated within a variational approach to density functional perturbation theory [20]. Phonon dispersion curves are interpolated according to the scheme described by Gonze *et al.* [21]. In this scheme, the dipole-dipole interactions are subtracted from the dynamical matrices before Fourier transformation, so that only the short-range part is handled in real space. A 4 × 4 × 4 q-points grid in the irreducible Brillouin zone is employed for the calculation of the vibrational band structure while a denser 100 × 100 × 80 grid is used for the calculation of the phonon density-of-states and the thermodynamic functions. The

Raman susceptibility tensors are obtained within a nonlinear response formalism, making use of the $2n+1$ theorem [22]. The infrared transmittance, infrared reflectivity and Raman spectra are calculated as described in Refs. [23–25], respectively.

In our calculations, the orthogonal reference system (x,y,z) is chosen such as z is aligned along the C_6-axis and x is aligned along the crystallographic a-axis.

IV. RESULTS AND DISCUSSION

A. Raman measurements on polycrystalline samples

Unlike infrared spectroscopy, relative band intensities within a Raman spectrum are largely unaffected by powder particle size and packing density. They do have some influence on the overall intensity, hence the signal to noise ratio, of a Raman spectrum. The position of the Raman lines is also influenced by the particle size. However, according to Table I, the frequency shift of the Raman lines is weak between polycrystalline powders, single crystals, or thin films.

Fig. 1 reports the Raman spectra of our polycrystalline $CrSi_2$ sample at room temperature and using two laser line excitations: $\lambda = 531$ nm (green) and $\lambda = 633$ nm (red). These spectra are normalized to the highest intensity line at 307 cm^{-1}. We observe that the intensity of the doublet in the 395-415 cm^{-1} range is strongly dependent of the laser line excitation. This phenomenon has been checked on a large number of samples and could be attributed to a resonant (or quasi-resonant) effect. In addition, this effect highlights the two lines centered at 233 and 251 cm^{-1} measured using the red laser. Only the first line has been reported in previous Raman works [2, 12, 14] as they were performed using a green laser. So, these findings call in question the mode assignment reported in the literature. This will be further discussed in section IV.D.

In order to understand the anharmonicity of the lattice vibrations, we have performed Raman experiments between room temperature and 500°C (see Fig. 2). Temperature dependence of the most intense Raman lines is displayed in Fig. 3. Their frequency decreases linearly as a function of temperature. There are two different contributions to the temperature dependence of the Raman shifts [26]: the explicit ($\omega_{expl.}$) and the implicit ($\omega_{impl.}$) volume-contributions. The first one comes from the 3- and 4-phonons interactions, while the

second one can be calculated using the volume thermal expansion (β_V) and the Grüneisen parameter (γ_m) of a specific Raman mode m. At high-temperature and under the isotropic approximation, the implicit contribution varies linearly with the temperature as:

$$\omega_{impl.} = \omega_{0m}(1 - \gamma_m \beta_V T), \quad (1)$$

where ω_{0m} is the Raman frequency shift of the mode m at 0 K. Here, we are interested to compare the slopes of the different Raman modes with the expected slope for the implicit contribution alone. The accurate determination of γ_m requires Raman experiments under pressure and on single-crystal. However, because these experiments are not available, one makes the approximation to use, instead of γ_m, the thermodynamic Grüneisen parameter defined as: $\Gamma = \frac{\beta_V B V}{C_p}$, where B, V and C_p are the bulk modulus, the volume and the experimental heat capacity, respectively. Using the experimental mesurements of β_V and C_p from Dasgupta *et al.* [7] and the elastic constants measured by Nakamura *et al.* [27], we found $\Gamma \approx 2$ at room temperature. This value decreases to $\Gamma \approx 1.8$ at 600 K. Substituting γ_m by Γ in Eq. (1) and using $\beta_V = 3.62\times10^{-5}$ K^{-1}, one gets a slope normalized to ω_{0m} of 6.5 to 7.2×10^{-5} K^{-1}. As we can see in Fig. 3, these values are very close to the experimental values obtained for the modes at 230 and 310 cm^{-1}, but are 20% larger than for the three modes at the highest energies [28]. Consequently, the present results could suggest that the temperature dependence of the Raman shift is dominated by the volume contribution. This result is related to the quite large Grüneisen parameter found in $CrSi_2$ and, as we will see later, it will have a strong impact for explaining its thermal conductivity.

B. Optical dielectric tensor

The electronic dielectric permittivity tensor, ε^{∞}, describes the response of the electron gas to a homogeneous electric field if the ions are taken as fixed at their equilibrium positions. No scissor correction has been used in the calculation of this tensor. Due to the hexagonal symmetry, ε^{∞} is diagonal with two independent components labelled: $xx = yy = \perp$ and $zz = \parallel$. Our calculations give: $\varepsilon^{\infty}_{\perp} = 31.16$ and $\varepsilon^{\infty}_{\parallel} = 26.50$, corresponding to an ordinary optical refractive index, n_o =5.58, and an extraordinary refractive index, n_e =5.14. $CrSi_2$ is therefore a negative uniaxial crystal with a quite isotropic electronic response to a homogeneous electric field. Their calculated mean values, $\bar{\varepsilon^{\infty}}$ =30 and $\bar{n}$ =5.4, are consistent

with the corresponding experimental ones: $30 \leq \varepsilon^{\infty} \leq 43$ (refs. [13] and [2]) and $\bar{n} = 5.3$ ([1]). This is a consequence of the good agreement between the calculated and measured band gap energy.

C. Phonon dispersion curves and density-of-states

Phonon dispersion curves give a criterion for the crystal stability and indicate, through the prediction of soft modes, the possible phase transitions. Indeed, if all phonon frequencies are positive, the crystal is locally stable. However, if it appears that some frequencies are imaginary (soft modes), then the system is unstable. The phonon dispersion curves of $CrSi_2$ are displayed in Fig. 4 along high-symmetry directions. No soft mode is predicted by our calculations in the whole Brillouin zone, suggesting that the compound is thermodynamically stable at ambient pressure and 0 K. The contribution of each kind of atom to each phonon branch is also displayed in this figure using a color code. We observe that pure atomic motions of Si-atoms dominate the modes above 350 cm^{-1}, while pure atomic motions of Cr-atoms contribute around 300 cm^{-1}. For the other frequencies, collective atomic motions of Cr and Si-atoms are involved. The acoustic branches show a significant dispersion and they exhibit a noticeable mixing with the first low-frequency optical branches in the whole Brillouin zone. Thus, this compound has interesting thermal expansion properties, which have been measured by Dasgupta *et al.* [7]. The atomic contributions to phonon acoustic mode come from collective motions of Cr and Si-atoms. In contrast, the optical phonon branches are quite dispersionless except at high frequency. The maximum value of the phonon frequencies is close to the K high-symmetry point. We do not observe a clear gap between the optical branches. As a consequence, the phonon density-of-states spectrum has a quite continuous profile with a complex multipeak structure between 100 and 470 cm^{-1} (see Fig. 5). The low density of modes at low frequencies up to the first peak around 170 cm^{-1} suggests a stiffness of the $CrSi_2$ lattice [29]. This peak is mainly due to the lowest energy transverse acoustic (TA) mode at the Brillouin zone boundaries (at K and M high-symmetry points). The constant-volume heat capacity (C_v) has been also derived from the knowledge of the phonon density-of-states (inset of Fig. 5). At high temperatures, the specific heat approaches the classical Dulong and Petit asymptotic limit: $C_v(T \to \infty) = 74.83$ $J.mol^{-1}.K^{-1}$. The linear fit of C_v with respect to T^3 at very low tem-

peratures ($T < 10$ K) gives access to an estimation of the Debye temperature. As a rule of thumb, a higher Debye temperature implies a higher associated thermal conductivity. We find a calculated Debye temperature, θ_D^{calc} =766 K, in fair agreement with the experiment [27] (θ_D^{exp} =793 K). This Debye temperature is relatively high and similar to that of diamond silicon and could suggest a good thermal conductivity of $CrSi_2$. However, the thermal conductivity of $CrSi_2$ is about one order of magnitude smaller [7] (∼10 W/m.K) than that of the diamond silicon [30] (∼156 W/m.K). This can not be easily explained by the larger average mass and the larger number of atoms in the $CrSi_2$ primitive cell. In order to explain this difference, the anharmonicity should be higher in $CrSi_2$ than in diamond silicon. A good measure of the crystal anharmonicity comes from their mode Grüneisen parameter [31]. As previously discussed, the Grüneisen parameter of $CrSi_2$ is much larger than in silicon where it is 0.56 at high temperatures [31]. The Umklapp scattering model for calculating the thermal conductivity at high temperatures as proposed by Slack (see equation 7.2 in [31]), associated with the experimental Debye temperature [27] and the Grüneisen parameter of about 2, gives at room temperature κ =24 W/m.K for $CrSi_2$. This value is the same order of magnitude than in the experiments and one order of magnitude lower than the thermal conductivity of silicon. Note that it is not unusual to overestimate the thermal conductivity by the Slack's model [31, 32]. Some other thermoelectrics, such as the antifluorite Mg_2X compounds (with X = Si, Ge or Sn) with similar thermal conductivity, have much lower Debye temperature than $CrSi_2$ but also lower Grüneisen parameter (≈1.3-1.4) [31]. Clearly, the relatively low thermal conductivity of $CrSi_2$ is due to the compensation of its high Debye temperature by its relatively high Grüneisen parameter. Therefore, an efficient way to decrease the thermal conductivity of $CrSi_2$ would be to reduce its Debye temperature by alloying it with heavier atoms. In addition, the alloying will increase short wavelength phonon scattering. As discussed by Vineis *et al.* [33], combinations of alloying and wide size distribution of nanoparticles is preferable to effectively scatter different phonon modes and reduce the thermal conductivity. We suggest that this approach will be even more efficient in $CrSi_2$ when it will be alloyed with heavy atoms because not only alloying will increase the phonon scattering but it will also decrease the sound velocity and then will further reduce the thermal conductivity.

D. Infrared and Raman spectroscopies

Despite of several experimental investigations of the $CrSi_2$ lattice dynamics, the assignment of its zone-center phonon modes is not yet unambigously established in the literature, especially below 320 cm^{-1}. This controversy is mainly due (i) to the difficulty to make high-quality single crystals and (ii) to the fact that the assignments are performed analyzing the counterpart modes in the experimental infrared and Raman spectra ($CrSi_2$ is a noncentrosymmetric structure). The experimental phonon frequencies reported in the literature using infrared and Raman spectrocopies are listed in Table I.

At the zone-center, optical phonon modes of $CrSi_2$ can be classified, according to the irreducible representations of the D_6 point group, into: $\Gamma_{opt} = A_1 \oplus 2A_2 \oplus 4E_2 \oplus 4E_1 \oplus 3B_2 \oplus 2B_1$. The E_1-modes are both infrared and Raman active and they are polarized in the $x-y$ plane. The A_1 and E_2-modes are Raman active, whereas the A_2-modes are infrared active and polarized along the z-direction. The B_1 and B_2-modes are silent. Their frequencies are calculated at 204 and 300 cm^{-1} (B_1-modes), and 238, 284 and 393 cm^{-1} (B_2-modes). They can however not be compared to experimental values since no experimental inelastic neutron scattering data are presently available. Close to the Γ-point, the macroscopic electric field splits the polar active modes into transverse (TO) and longitudinal (LO) modes (see Table II). The LO frequencies are calculated [20] from the TO frequencies with the additional knowledge of the Born effective charges and ε^{∞}. Thus, their predictions should be reliable.

The analyze of the infrared reflectivity spectra allows to quantify the LO-TO splitting strength. These spectra are calculated at normal incidence and they are displayed in Fig. 6 (left panels). The reflectivity saturates to the unity because our formalism neglects the damping of the phonon modes. We observe a large LO-TO splitting (more than 50 cm^{-1}) for the E_1(TO) modes centered at 336 cm^{-1} and for the A_2(TO) mode centered at 361 cm^{-1}. The eigenvectors of the polar TO modes do not necessarily correspond to those of their corresponding LO modes due to the long-range Coulomb interactions. We calculated the overlap matrix between the eigenvectors of the TO and LO as follows:

$$\langle \mathbf{u}_m^{LO} | M | \mathbf{u}_n^{TO} \rangle = \sum_{\gamma,\kappa} u_m^{LO}(\kappa\gamma) M_\kappa u_n^{TO}(\kappa\gamma), \quad (2)$$

where M_κ is the mass of the κ^{th}-atom, and $\mathbf{u}_m^{LO}$ and $\mathbf{u}_n^{TO}$ are the eigendisplacement vectors of the m^{th} LO and n^{th} TO modes, respectively. This overlap is strong for the E_1(LO2) mode

(see Table III). As a consequence, the eigenvector of the E_1(LO2) is a mixing of those of the E_1(TO2) and E_1(TO3) modes. In contrast, the eigenvector of the E_1(LO1), E_1(LO3) and E_1(LO4) modes can be associated at the first order to the E_1(TO1), E_1(TO3) and E_1(TO4) eigenvectors, respectively. Similarly, the overlap matrix between the A_2(TO) and A_2(LO) modes shows that their mixing is strong (see Table IV).

Fig. 7 displays the calculated non-resonant spectrum of a $CrSi_2$ ploycrystalline compound. In practice, this average is performed by evaluating the Raman tensor components for an arbitrary orientation in space using Euler angles [34]. The experimental spectrum, recorded at room temperature and using the 633 nm laser line excitation, is also reported on this figure. As expected, we observe a poor agreement between the calculated and experimental relative intensity of the Raman lines due to resonant (or quasi-resonant) effect. This effect does not alter the frequency position of the Raman lines but enhances their intensities as highlighted in Fig. 1, leading the relative intensity of the calculated Raman lines unmeaningful. However, the assignment of the Raman lines is still possible using first-principles based methods because the number of experimental Raman active mode and their frequency position are in qualitative good agreement with the calculated ones. This assignment is symbolized by the dashed lines in the figure. The observed frequency shift of the lines between the experiment and the calculation is related to the anharmonicity of modes that is not included in our calculations.

The calculated and experimental infrared transmittance spectrum are displayed in Fig. 6 (right panel) for a polycrystalline compound. In this configuration only the TO modes are sensitive. The experimental infrared spectrum is dominated as expected by six infrared bands at 229, 252, 290, 297, 355 and 382 cm^{-1}. The strong band at 355 cm^{-1} with a shoulder on its high-frequency side at 382 cm^{-1}, is correctly calculated both in position and relative intensity. The doublet around 295 cm^{-1} is not distinctly observed in the calculated spectrum because we use a constant linewidth (5 cm^{-1}) to represent the bands, but it appears when we decrease this linewidth at 1 cm^{-1} (see inset B of Fig. 6). While this doublet is always observed by the authors, its relative intensity can change. Indeed, the relative intensity of the high-frequency component appears smaller on the calculated spectrum than on the experimental one recorded by Chaix-Pluchery *et al.* [12]. However, it is well reproduced by our calculation when we consider the experimental spectrum recorded by Borghesi *et al.* [14]. The bands centered at 252 and 229 cm^{-1} are well reproduced by our calculation and the

latter has the smallest intensity. Thus, this good agreement calculation-experiment suggests a reliable assignment of the infrared modes.

In agreement with the literature, the experimental bands centered at 229, 297 and 355 cm^{-1} are assigned as E_1, while the line at 382 cm^{-1} is assigned as A_2. For the two remaining infrared experimental bands (290 and 252 cm^{-1}), we suggest a revisited assignment that the one reported in the literature (see Tables I and II). Indeed, Chaix-Pluchery *et al.* [12] and Borghesi *et al.* [14] have assigned the band at 290 cm^{-1} as E_1 because a weak and broad Raman line can be observed close to this frequency. However, our calculations support that this mode is in fact two distinct modes: the first one is infrared active (calculated at 280 cm^{-1}) and assigned as A_2, while the second one is Raman active (calculated at 291 cm^{-1}) and assigned as E_1(LO). This E_1(LO) line should undergo a frequency dispersion as a function of angle between the phonon wavevector and the $CrSi_2$ basal plane (estimated $\sim$10 cm^{-1} by our calculation). As a consequence, this revisited assignment could be unambiguously checked with the measure of this frequency angular dependence using Raman spectroscopy on single crystal. Similarly, Chaix-Pluchery *et al.* [12] and Borghesi *et al.* [14] have assigned the infrared band at 252 cm^{-1} as A_2 because it has no counterpart in the Raman spectrum. However, we assigned this band as E_1(TO) because (i) a weak line can be observed at 252 cm^{-1} in the experimental Raman spectrum of Chaix-Pluchery *et al.* [12] recorded using the 514.5 nm laser line in the $y(xx)\bar{y} + \epsilon\ y(xz)\bar{y}$ configuration with $0.2 \leq \epsilon \leq 0.3$ (Fig. 5c of their paper), and (ii) a weak and broad line at 252 cm^{-1} can be observed in our experimental Raman spectra using the 633 nm laser line (see also Fig. 1). The four Raman active E_2 modes and the A_1 mode are unambiguously assigned by our calculations and this assignment is consistent with the literature. Our revisited assignment of the $CrSi_2$ phonon modes is summarized in Table II.

E. Static dielectric constant

The static dielectric constant of $CrSi_2$ can be estimated theoretically, adding to the purely electronic response, the contribution coming from the response of the crystal lattice. To estimate this last contribution, one can use a model that assimilates the solid to a system of undamped harmonic oscillators. Doing so, the static dielectric constant, ε^0, appears as the sum of an electronic contribution (ε^∞) and a contribution arising from each individual

polar phonon mode (ε_m^{ph}) such as [20, 24]:

$$\varepsilon^0_{\alpha\beta} = \varepsilon^\infty_{\alpha\beta} + \sum_m \varepsilon^{ph}_{\alpha\beta,m} = \varepsilon^\infty_{\alpha\beta} + \frac{4\pi}{\Omega_0} \sum_m \frac{S_{\alpha\beta}(m)}{\omega_m^2}, \quad (3)$$

where the sum runs over all modes m, the Greek indices denote the Cartesian components, Ω_0 is the unit cell volume and S is the infrared oscillator strength. Results of this decomposition are reported in Table V. The electronic and the phonon contributions each contribute to about half to the static dielectric constant. The phonon contribution of the E_1-modes is mainly governed by the modes centered at 249 and 336 cm^{-1}, and contribute around 20% each to $\varepsilon^0_\perp$. Similarly, the mode centered at 280 cm^{-1} dominates $\varepsilon^0_\parallel$ by about 37%.

F. Elastic constants and related mechanical properties

Elastic constants give interesting information on the nature of the forces operating in solids. In particular, they provide information on the stability and the stiffness of materials. Within the D_6 point group, elastic tensor has five independent elements to be determined: C_{11}, C_{12}, C_{13}, C_{33} and C_{44}. These independent elements have been calculated at 0 K according to the linear response formalism and using a fully relaxation (lattice parameters and atomic positions) of the $CrSi_2$ primitive unit cell. Our relaxed lattice parameters are: a =4.34 Å and c =6.27 Å. The elastic constants are listed in Table VI with the experimental ones measured at room temperature by Nakamura *et al.* [27], and an overall qualitative agreement is observed between the two sets. The discrepancies between the calculation and the experiment could be related to (i) the calculated equilibrium lattice constants that are slightly smaller then the experimental ones, (ii) the temperature effect, and (iii) the LDA because the calculation of elastic constants is observed to be dependent on the used functional. $CrSi_2$ is mechanically stable because the elastic constants satisfy Born mechanical stability restrictions for hexagonal structures, which are given by the following system of inequations [35, 36]: $C_{11} - |C_{12}| > 0$, $(C_{11} + 2C_{12})C_{33} - 2C_{13}^2 > 0$ and $C_{44} > 0$.

From the calculated elastic constants, we derived the macroscopic mechanical parameters, namely the bulk, shear and Young's moduli, using the Voigt-Reuss-Hill (H) approach [37]. It is known that the Voigt (V) bound is obtained by the average polycrystalline moduli based on an assumption of uniform strain throughout a polycrystal and is the upper limit of the actual effective moduli, while the Reuss (R) bound is obtained by assuming a uniform stress

and is the lower limit of the actual effective moduli [36, 37]. The explicit expressions of the bulk (B) and shear (G) moduli as a function of elastic constants for hexagonal structures are given in [36].

At the same time, we derived the Young modulus and Poisson ratio. All these mechanical properties are listed in Table VI. We observe that the parameter limiting the stability of $CrSi_2$ is the shear modulus as $G_X < B_X$, where $X = R, V, H$. The typical value of Poisson ratio is about 0.2 for covalent materials such as silicon whereas it is about 0.3-0.4 for ionic materials and 0.5 for pure-ionic limit [38]. In the present case, the calculated value of Poisson ratio is 0.18 (0.16 from the experiment) whatever the chosen approach. This suggests that the atomic bonding of $CrSi_2$ has a strong covalent character. The large negative Cauchy pressures (see [39] for the case of low symmetry systems), $P_z^{Cauchy} = C_{12}$-C_{66} ($\approx$ -118.1 GPa both from our calculations and from experiments [27]) and $P_x^{Cauchy} = C_{13}$-C_{44} ($\approx$ -54.2 GPa in our calculations and -66.5 GPa in experiments [27]), associated to this relatively small Poisson ratio indicate that the bondings have highly directional character (this is also the case for compounds with diamond structure [38, 39]). We note however that the Cauchy pressure is much more negative than in Si or Ge. This is certainly related to the very large values of the elastic constants in $CrSi_2$. From the above discussion, it is therefore not surprising to find that $CrSi_2$ is very brittle because its B/G ratio is only of 1.25. Indeed, the brittle or ductile behavior of a material can be estimated according to the value of the B/G ratio, as proposed by Pugh [40]. If $B/G > 1.75$, a ductile behavior is predicted, otherwise the material behaves in a brittle manner. This result agrees well with the experiments.

G. Piezoelectric properties

Finally, we report the piezoelectric constants of $CrSi_2$ to complete its mechanical properties. Within the D_6 point group, there is only one independent piezoelectric coefficient to be calculated. We found a piezoelectric-stress of e_{41} =0.31 C/m^2 and a piezolectric-strain of d_{41} =1.79 pC/N. There is no experimental value of these coefficients reported on $CrSi_2$ in the literature. However, for comparison with other binary compounds, we underline that α-quartz is presently the most used piezoelectric material with a piezoelectric-strain of d_{11}= 2.31 pC/N [41]. Nevertheless, its $\alpha - \beta$ phase transition at 846 K restricts its applications. The α-quartz phase of GeO_2 does not have a $\alpha - \beta$ phase transition [42] and its piezoelectric-

strain, d_{11} =5.72 pC/N, is more than twice that of α-quartz [43]. This piezoelectric activity is observed until at 1273 K. Thus, the sizable piezoelectric response of $CrSi_2$, associated to its thermal stability (*i.e.* no phase transition observed up to its melting temperature about 1750 K), could make this compound an interesting piezoelectric. This prediction requires experimental confirmations.

V. CONCLUSIONS

In this article, we have reported a complete study of the lattice dynamics, dielectric, elastic and piezolectric properties of the hexagonal semiconducting $CrSi_2$. First, we observed that the experimental Raman of $CrSi_2$ shows a resonant character and that the temperature dependence of the Raman frequencies is mainly due to an implicit volume contribution, leading to large Grüneisen parameter. The latter can also explain why $CrSi_2$ has a moderate thermal conductivity, although it has quite large Debye temperature. Consequently, an efficient way for reducing its thermal conductivity could be to reduce its Debye temperature by alloying it with large amounts of heavy atoms as not only this will increase the scattering of the phonons but also will decrease their velocity. This kind of alloying is expected to be more efficient than in cubic Mg_2Si where few percent of Ge substitution on Si lead to a decrease of the thermal conductivity by a factor 2 to 3 (Ref. [44]). Indeed, even if $CrSi_2$ and Mg_2Si have a similar thermal conductivity, Mg_2Si has a lower Debye temperature and Gruneisen parameter.

Then, we have revisited the zone-center phonon assignments of $CrSi_2$ from the combination of our Raman measurements and our calculations, so that the contradictions met in the previous experimental studies concerning the vibration modes between 250 and 300 cm^{-1} are now explained and understood. We suggest that the experimental Raman line centered at 290 cm^{-1} assigned as E_1 in the literature is in fact two distinct modes: the first one is infrared active (calculated at 280 cm^{-1}) and assigned as A_2, while the second one is Raman active (calculated at 291 cm^{-1}) and assigned as E_1(LO). This E_1(LO) line should undergo a frequency dispersion as a function of angle between the phonon wavevector and the $CrSi_2$ basal plane (estimated $\sim$10 cm^{-1} by our calculation). As a consequence, this revisited assignment could be unambiguously checked with the measure of this frequency angular dependence using Raman spectroscopy on single crystal. Similarly, we suggest that

the experimental infrared band at 252 cm^{-1} is assigned as E_1(TO) instead of A_2 as reported in the literature. The static dielectric constant of $CrSi_2$ was also analyzed and our calculations show that the electronic and the phonon contributions each contribute to about half.

Finally, the calculation of the piezoelectric coefficient of $CrSi_2$ shows a sizable value with a magnitude similar to that reported for α-quartz. This prediction requires, however, experimental confirmations. Thus, compounds with the same hexagonal symmetry than $CrSi_2$ (*i.e.* $P6_222$) could be interesting for piezoelectric applications, especially those with an energy band gap larger than in $CrSi_2$.

Acknowledgements

This work was realized with the support of HPC@LR, a Center of Competence in High-Performance Computing from the Languedoc-Roussillon region, funded by the Languedoc-Roussillon region, Europe and Université Montpellier 2.

[1] M. C. Bost, J. E. Mahan. An investigation of the optical constants and band gap of chromium disilicide. *J. Appl. Phys.* **63** (1988) 839-844.

[2] H. Lange, M. Giehler, W. Henrion, F. Fenske, I. Sieber, G. Oertel. Growth and Optical Characterization of $CrSi_2$ Thin Films. *Phys. Stat. Sol. (b)* **171** (1992) 63-75.

[3] H. Lange. Electronic Properties of Semiconducting Silcides. *Phys. stat. sol. (b)* **201** (1997) 3-65.

[4] V. K. Zaitsev, M. I. Fedorov, E. A. Gurieva. Thermoelectrics on the Base of Solid Solutions of Mg_2B^{IV} Compounds (B^{IV} = Si, Ge, Sn). *Thermoelectric Handbook - macro to nano*, CRC Press, Taylor & Francis, 2006, ch. 29 and refs. therein.

[5] M. I. Fedorov, V. K. Zaitsev. Thermoelectrics of Transition Metal Silicides. *Thermoelectric Handbook - macro to nano*, CRC Press, Taylor & Francis, 2006, ch. 31 and refs. therein.

[6] W. Liu, X. Tan, K. Yin, H. Liu, X. Tang, J. Shi, Q. Zhang, C. Uher. Convergence of Conduction Bands as Means of Enhancing Thermoelectric Performance of n-Type $Mg_2Si_{1-x}Sn_x$ Solid Solutions. *Phys. Rev. Lett.* **108** (2012) 166601.

[7] T. Dasgupta, J. Etourneau, B. Chevalier, S. F. Mater, A. M. Umarji. Structural, thermal, and electrical properties of $CrSi_2$. *J. Appl. Phys.* **103** (2008) 113516.

[8] T. Dasgupta, A. M. Umarji. Role of milling parameters and impurity on the thermoelectric properties of mechanically alloyed chromium silicide *J. Alloys Compd.* **461** (2008) 292-297.

[9] T. Pandey, A. K. Singh. Role of milling parameters and impurity on the thermoelectric properties of mechanically alloyed chromium silicide *RSC Adv.* **4** (2014) 3482-3486.

[10] D. Parker D. J. Singh. Very heavily electron-doped CrSi2 as a high-performance high-temperature thermoelectric material *New J. Phys.* **14** (2012) 033045.

[11] S. Karuppaiah, M. Beaudhuin, R. Viennois. Investigation on the thermoelectric properties of nanostructured $Cr_{1-x}Ti_xSi_2$ *J. Solid State Chem.* **199** (2013) 90-95.

[12] O. Chaix-Pluchery, G. Lucazeau. Vibrational Study of Transition Metal Disilicides, MSi_2 (M=Nb, Ta, V, Cr). *J. Raman Spectrosc.* **29** (1998) 159-164.

[13] V. Bellani, G. Guizzetti, F. Marabelli, A. Piaggi, A. Borghesi, F. Nava, V. N. Antonov, VI. N. Antonov, O. Jepsen, O. K. Andersen, V. V. Nemoshkalenko. Theory and experiment on the optical properties of $CrSi_2$. *Phys. Rev. B***46** (1992) 9380-9388.

[14] A. Borghesi, A. Piaggi, A. Franchini, G. Guizzetti, F. Nava, G. Santoro. Far-Infrared Vibrational Spectroscopy in $CrSi_2$ *Europhys. Lett.* **11** (1990) 61-65.

[15] X. Gonze, B. Amadon, P. M. Anglade, J. M. Beuken, F. Bottin, P. Boulanger, F. Bruneval, D. Caliste, R. Caracas *et al.* ABINIT: First-principles Approach to Material and Nanosystem Properties. *Comput. Phys. Comm.* **180** (2009) 2582-2615.

[16] J. P. Perdew, Y. Wang. Accurate and Simple Analytic Representation of the Electron-gas Correlation Energy. *Phys. Rev. B* **45** (1992) 13244-13249.

[17] N. Troullier, J. L. Martins. Efficient Pseudopotentials for Plane-wave Calculations. *Phys. Rev. B* **43** (1991) 1993-2006.

[18] H. J. Monkhorst, J. D. Pack. Special Points for Brillouin-zone Integrations. *Phys. Rev. B* **13** (1976) 5188-5192.

[19] W. Henrion, H. Lange, E. Jahne, M. Giehler. Optical Properties of Chromium and Iron Disilicide Layers. *Appl. Surf. Sci.* **70/71** (1993) 569-572.

[20] Gonze, X.; Lee, C. Dynamical matrices, Born effective charges, dielectric permittivity tensors, and interatomic force constants from density-functional perturbation theory. *Phys. Rev. B* **55** (1997) 10355-10368.

[21] X. Gonze, J.-C. Charlier, D. C.; Allan, M. P. Teter. Interatomic Force Constants From First Principles: The Case of α-quartz. *Phys. Rev. B* **50** (1994) 13035-13038.

[22] M. Veithen, X. Gonze, Ph. Ghosez. First-Principles Study of the Electro-Optic Effect in Ferroelectric Oxides. *Phys. Rev. Lett.* **93** (2004) 187401.

[23] P. Hermet, J.-L. Bantignies, A. Rahmani, J.-L. Sauvajol, M. R. Johnson, F. Serein. Far- and Mid-Infrared of Crystalline 2,2'-Bithiophene: Ab Initio Analysis and Comparison with Infrared Response. *J. Phys. Chem. A* **109** (2005) 1684-1691.

[24] P. Hermet, L. Gourrier, J.-L. Bantignies, D. Ravot, T. Michel, S. Deabate, P. Boulet, F. Henn. Dielectric, Magnetic, and Phonon Properties of Nickel Hydroxide. *Phys. Rev. B* **84** (2011) 235211.

[25] P. Hermet, M. Veithen, Ph. Ghosez. First-principles Calculations of the Nonlinear Optical Susceptibilities and Raman Scattering Spectra of Lithium Niobate. *J. Phys.: Condens. Matter* **19** (2007) 456202.

[26] G. Lucazeau. Effect of pressure and temperature on Raman spectra of solids: anharmonicity. *J. Raman Spectrosc.* **34** (2003) 478-496.

[27] M. Nakamura. Elastic Constants of Some Transition-Metal-Disilicide Single-Crystals. *Met. Mat. Trans. A* **25** (1994) 331-340.

[28] As can be seen in Fig. 3, one can note that the energy of the Raman mode at 300 cm^{-1} decreases linearly as a function of temperature with a a slope normalized to ω_{0m} of about 5.9×10^{-5} K^{-1}. However, the error bar for this mode is large due to its overlapping with the Raman mode at 308 cm^{-1}. We estimate the error bar for the slope to be about 20% and therefore we are not able to conclude anything about the behavior of this mode with the temperature.

[29] P. Hermet, K. Niedziolka and P. Jund. A first-principles investigation of the thermodynamic and mechanical properties of Ni-Ti-Sn Heusler and half-Heusler materials. *RSC Adv.* **3** (2013) 22176-22184.

[30] C. J. Glassbrenner, G. A. Slack. Thermal Conductivity of Silicon and Germanium from 3°K to the Melting Point. *Phys. Rev.* **134** (1964) A1058-A1069.

[31] G. A. Slack. The Thermal Conductivity of Nonmetallic Crystals *Solid State Phys.* **34** (1979) 1-71.

[32] L. Bjerg, B. B. Iversen, G. K. H. Madsen. Modeling the thermal conductivities of the zinc antimonides ZnSb and Zn_4Sb_3. *Phys. Rev. B* **89** (2014) 024304.

[33] C. J. Vineis, A. Shakouri, A. Majundar, G. Kanatzidis. Nanostructured Thermoelectrics: Big Efficiency Gains from Small Features *Adv. Mat.* **22** (2010) 3970-3980.

[34] H. Djani, P. Hermet, P. Ghosez. First-Principles Characterization of the $P2_1ab$ Ferroelectric Phase of Aurivillius Bi_2WO_6 *J. Phys. Chem. C* **118** (2014) 13514-13524.

[35] M. Born. On the stability of crystal lattices I. *Proc. Cambridge Philos. Soc.* **36** (1940) 160-172.

[36] Z. J. Wu, E. J. Zhao, H. P. Xiang, X. F. Hao, X. J. Liu, J. Meng. Crystal structures and elastic properties of superhard IrN_2 and IrN_3 from first principles. *Phys. Rev. B* **76** (2007) 054115.

[37] H. Ledbetter. Monocrystal-polycrystal elastic constant models. *Handbook of Elastic Properties of Solids, Liquids, and Gases, vol. III: Elastic Properties of Solids: Biological and Organic Materials, Earth and Marine Sciences* (2001) 313-324.

[38] H. Ledbetter. Poisson ratio and covalency-ionicity tetrahedral semiconductors. *Handbook of Elastic Properties of Solids, Liquids, and Gases, vol. II: Elastic Properties of Solids: Theory, Elements and Compounds, Novel Materials, Technological Materials, Alloys, and Building Materials* (2001) 281-287.

[39] S. Ganeshan, S. Shang, H. Zhang, Y. Wang, M. Mantina, Z. K. Liu. Elastic constants of binary Mg compounds from first-principles calculations. *Intermet.* **17** (2009) 313-318.

[40] S. F. Pugh. Relations between the elastic moduli and the plastic properties of polycrystalline pure metals. *Philos. Mag.* **45** (1954) 823-843.

[41] P. Armand, S. Clement, D. Balitsky, A. Lignie, P. Papet. Large SiO_2-substituted GeO_2 single-crystals with the α-quartz structure. *J. Cryst. Growth* **316** (2011) 153-157.

[42] G. Fraysse, A. Lignie, P. Hermet, P. Armand, D. Bourgogne, J. Haines, B. Ménaert, P. Papet. Vibrational origin of the thermal stability in the highly distorted α-quartz-type material GeO_2: an experimental and theoretical study. *Inorg. Chem.* **52** (2013) 7271-7279.

[43] A. Lignie, W. Zhou, P. Armand, B. Rufflé, R. Mayet, J. Debray, P. Hermet, B. Ménaert, P. Thomas, P. Papet. High-Temperature Elastic Moduli of Flux-Grown α-GeO_2 Single Crystal. *ChemPhysChem* **15** (2014) 118-125.

[44] W. L. Ren, C. C. Li, L. T. Zhang, K. Ito, J. S. Wu. Effects of Ge and B substitution on thermoelectric properties of CoSi. *J. Alloys Compds* **392** (2005) 50-54.

Raman				Infrared			
Present	[14]	[2]	[12]	[12]	[14]	[2, 19]	[13]
Powder	Film[c]	Film[d]	Single Crystal[d]	Film	Film	Film	Single crystal
233[b]			231 E_1	229 E_1	228 E_1	231	230
251[b]				**252 A_2**	**250 A_2**	**253**	**252**
	295–305 E_1	300	**290 E_1**	**290 E_1**	**295 E_1**	**295**	**296**
301[a,b]		300	300 E_1	297 E_1			
307[b]–311[a]		310	305 E_2				
						342	
			354 E_2				
357[a,b]	350–360 E_1	350	355 E_1	355 E_1	351 E_1	362	352
				382 A_2	375 A_2	381	370
399[a,b]		400	397 E_2				
413[a,b]		410	412 A_1				

[a] 531 nm laser line

[b] 633 nm laser line

[c] Laser line not reported

[d] 514.5 nm laser line

TABLE I: Zone-center phonon frequencies (in cm^{-1}) reported in the literature using Raman and infrared spectroscopies, together with their symmetry when available. Frequencies supposed with a wrong assignment are in bold.

	Calc.[a]	Exp. (cm^{-1})	
	(cm^{-1})	Raman	Infrared
E_1(TO1+LO1)	225	231-233[a,d]	228-231[b,c,d,e]
E_1(TO2)	249	251[a]	250-253[b,c,d,e]
E_1(LO2)	268		
A_2(TO2)	280		290-296[b,c,d,e]
E_1(TO3)	282	295-300[a,c,b]	297[d]
E_1(LO3)	291	290[d]	
E_2	311	305-311[a,b,d]	
A_2(LO1)	320		342[b]
E_2	338	354[d]	
E_1(TO4)	336	352-362[a,c,b,d]	350-360[b,c,d,e]
A_2(TO2)	361		370-382[b,c,d,e]
E_2	388	397-400[a,b,d]	
A_1	403	410-413[a,b,d]	
E_1(LO4)	440		
E_2	448		
A_2(LO2)	466		

[a]Present

[b]Refs. [2, 19]

[c]Ref. [14]

[d]Ref. [12]

[e]Ref. [13]

TABLE II: Revisited zone-center phonon mode assignment.

TABLE III: Overlap matrix between the eigenvectors of the E_1(LO) and E_1(TO) modes of $CrSi_2$. Values between parenthesis are the frequencies (in cm^{-1}) of the different modes whereas the values between brackets are the mode effective charges.

	TO1	TO2	TO3	TO4
E_1	[4.670]	[7.895]	[4.293]	[11.173]
	(225)	(249)	(282)	(336)
LO1 (230)	0.937	0.336	0.058	0.071
LO2 (268)	0.226	0.776	0.525	0.267
LO3 (291)	0.151	0.369	0.820	0.411
LO4 (440)	0.218	0.386	0.222	0.869

TABLE IV: Overlap matrix between the eigenvectors of the A_2(LO) and A_2(TO) modes of $CrSi_2$. Values between parenthesis are the frequencies (in cm^{-1}) of the different modes whereas the values between brackets are the mode effective charges.

	TO1	TO2
A_2	[11.241]	[9.050]
	(280)	(361)
LO1 (320)	0.808	0.589
LO2 (466)	0.589	0.808

	E_1-modes			A_2-modes		
	ω_m (cm^{-1})	S_m ($\times 10^{-4}$ $a.u.$)	$\varepsilon_{\perp}^{ph}$	ω_m (cm^{-1})	S_m ($\times 10^{-4}$ $a.u.$)	$\varepsilon_{\parallel}^{ph}$
	225	3.893	6.36	280	20.373	21.53
	249	10.384	13.90	361	14.969	9.51
	282	2.586	2.70			
	336	19.892	14.66			
Total (Phonons)			37.61			31.04
ε^{∞}			31.16			26.50
ε^{0}			68.77			57.54

TABLE V: Calculated transverse optical phonon contributions (ω_m) to static dielectric constant (ε^0) and mode oscillator strengths (S_m). Note: 1 $a.u.$ = 253.2638413 $m^3.s^{-2}$.

	Calc. Present	Exp. [27]		Calc. Present	Exp. [27]		Calc. Present	Exp. [27]		Calc. Present	Exp. [27]
C_{11}	454.0	372.2	B_V	219.99	172.29	B_R	219.68	171.73	B_H	219.84	172.01
C_{12}	72.6	45.3	G_V	177.31	153.59	G_R	176.44	153.03	G_H	176.88	153.31
C_{13}	118.5	82.6	B_V/G_V	1.24	1.12	B_R/G_R	1.25	1.12	B_H/G_H	1.24	1.12
C_{33}	453.0	385.2	ν_V	0.18	0.16	ν_R	0.18	0.16	ν_H	0.18	0.16
C_{44}	172.7	149.1	E_V	419.28	355.22	E_R	417.54	353.95	E_H	418.41	354.585

C_{66}=(C_{11}-C_{12})/2

TABLE VI: Calculated and experimental relaxed-ion (C) elastic constants, bulk (B), Young (E) and shear (G) moduli (in GPa), B_X/G_X ratio and Poisson coefficient (ν) using Voigt, Reuss and Hill approaches.

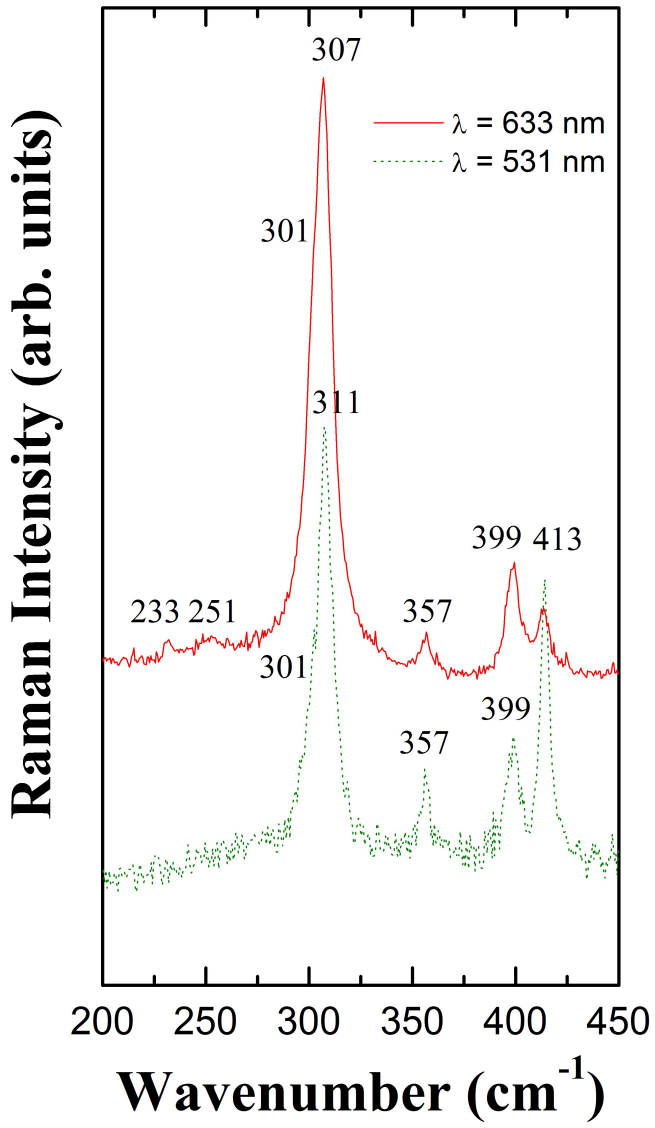

FIG. 1: Raman spectra of $CrSi_2$ polycrystals at room temperature and using two different laser line excitations.

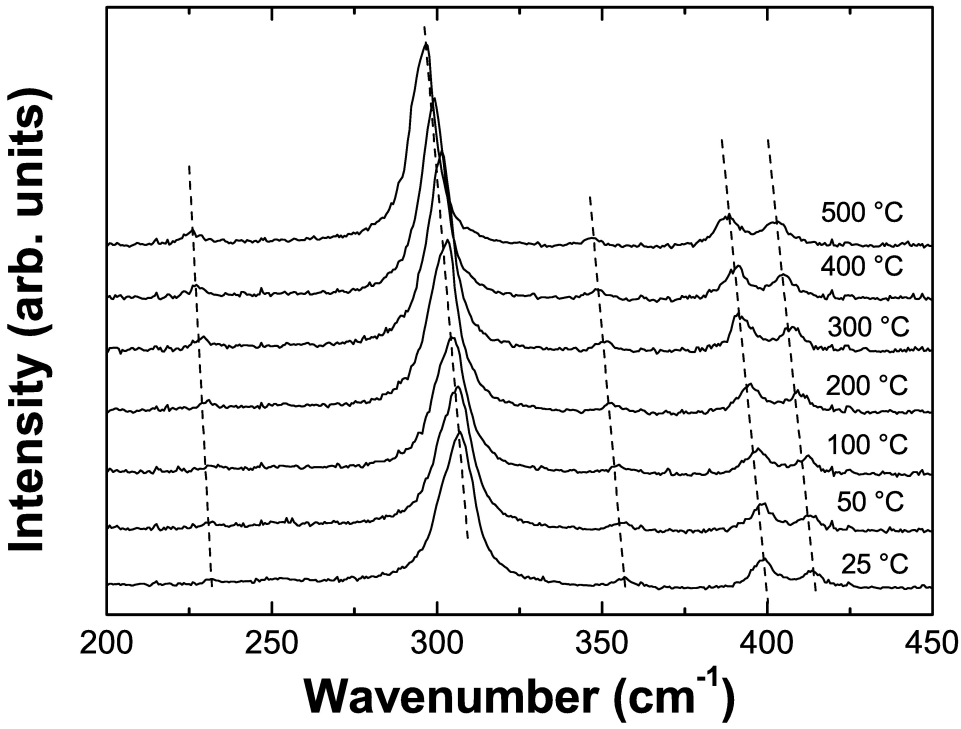

FIG. 2: Raman spectra of $CrSi_2$ polycrystals at different temperatures recorded using the 633 nm laser line. The dot lines highlight the frequency shift of the main lines.

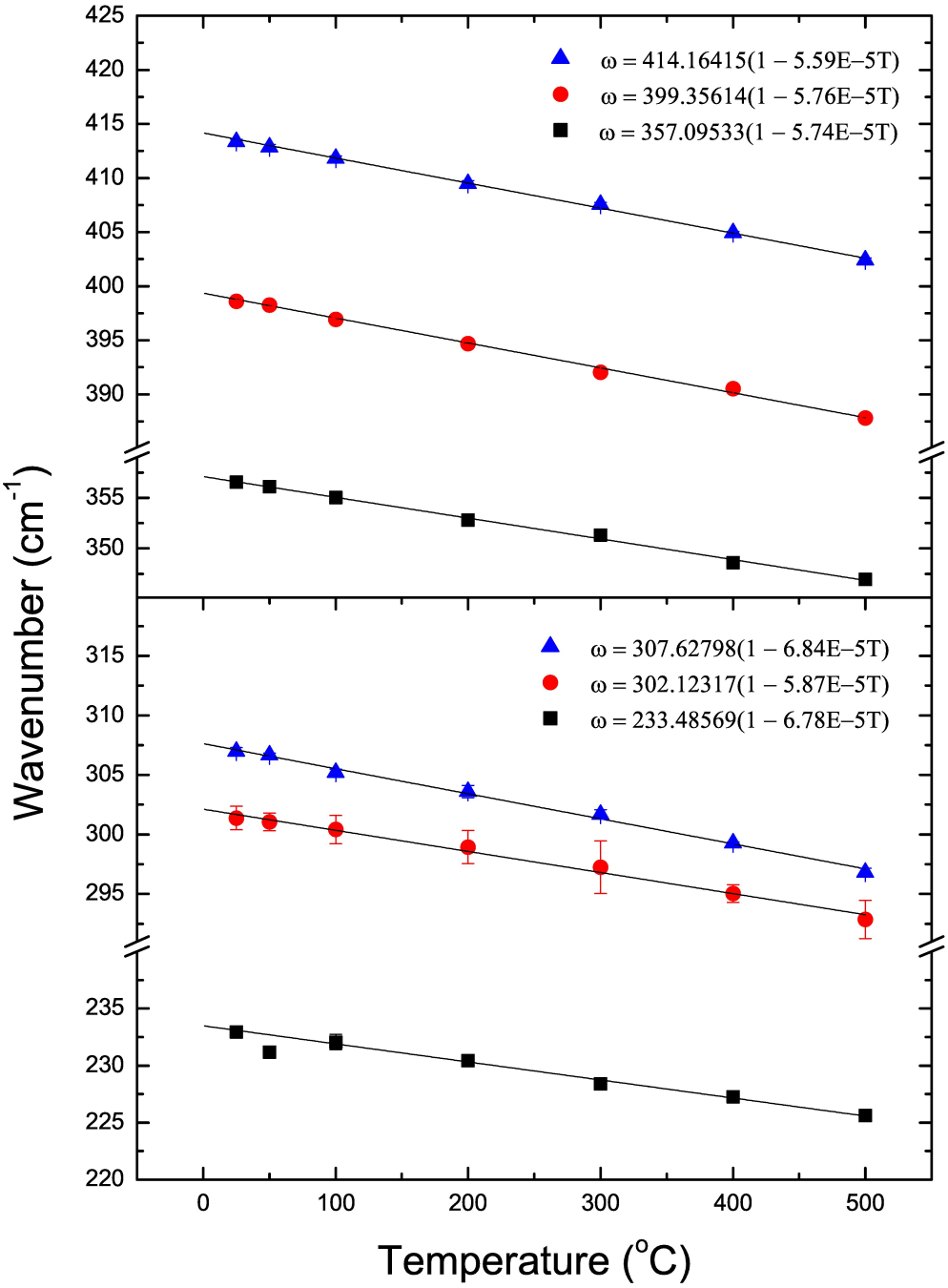

FIG. 3: Temperature dependence of the most intense Raman lines. Line equations are also given.

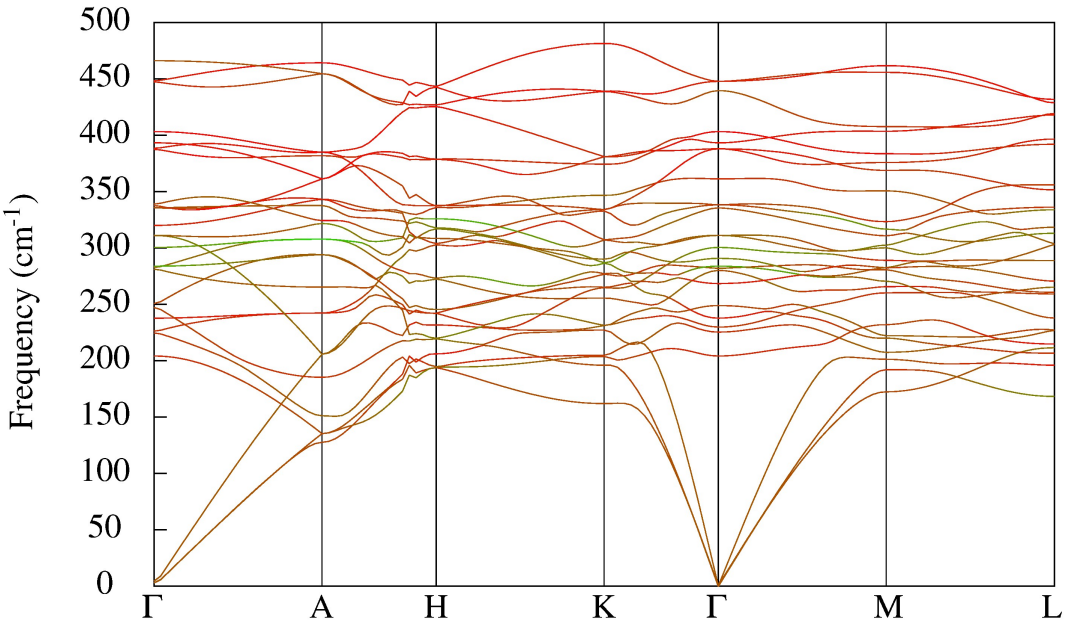

FIG. 4: Calculated phonon dispersion curves of $CrSi_2$. A color has been assigned to each point based on the contribution of each kind of atom to the associated dynamical matrix eigenvector: red for the Si-atoms and green for the Cr-atoms.

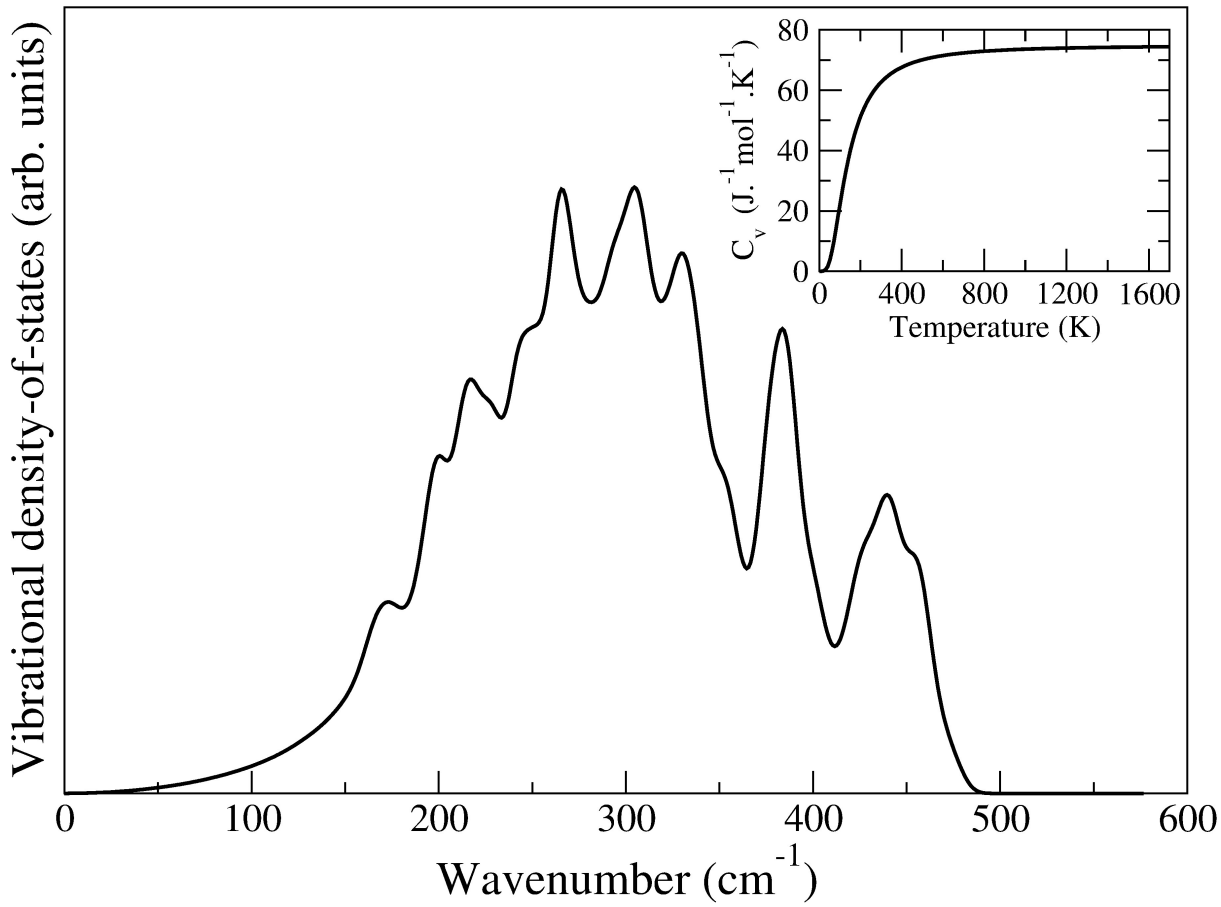

FIG. 5: Phonon density-of-states of $CrSi_2$. Inset: Calculated constant-volume heat capacity.

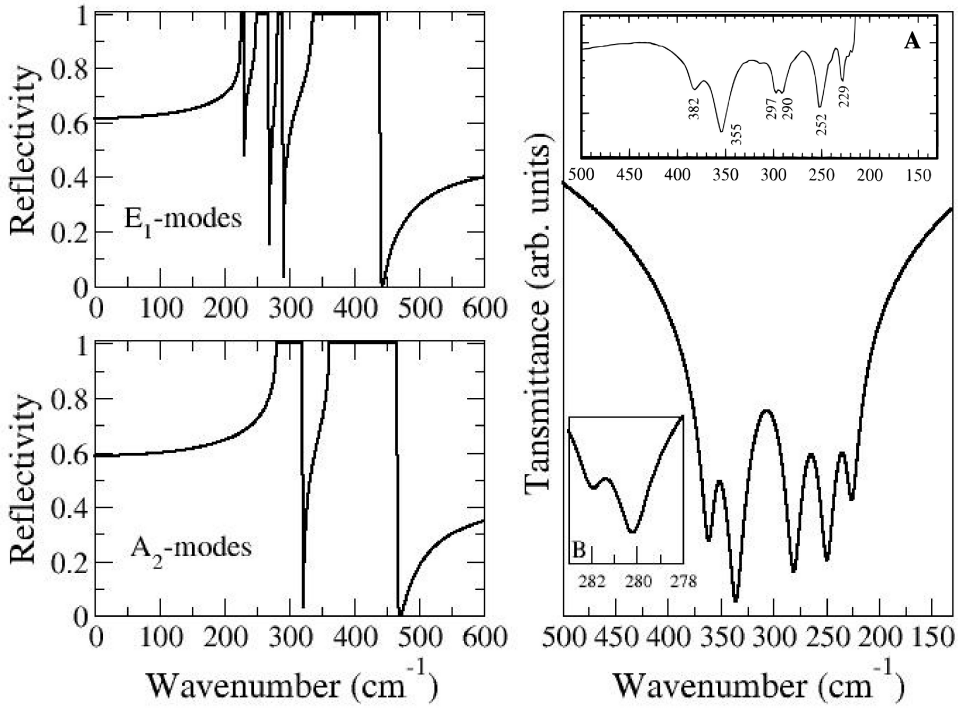

FIG. 6: Calculated infrared reflectivity spectra (left) of a $CrSi_2$ single-crystal and calculated infrared transmittance spectrum (right) of a $CrSi_2$ polycrystalline powder. We assume a Lorentzian line shape and a constant linewidth fixed at 5 cm^{-1} in the calculated infrared transmittance spectrum. Inset A: Experimental infrared transmittance spectrum on a polycrystalline film recorded by Chaix-Pluchery *et al.* [12]. Inset B: Calculated infrared spectrum in the 278-283 cm^{-1} range and using a smaller constant linewidth fixed at 1 cm^{-1}.

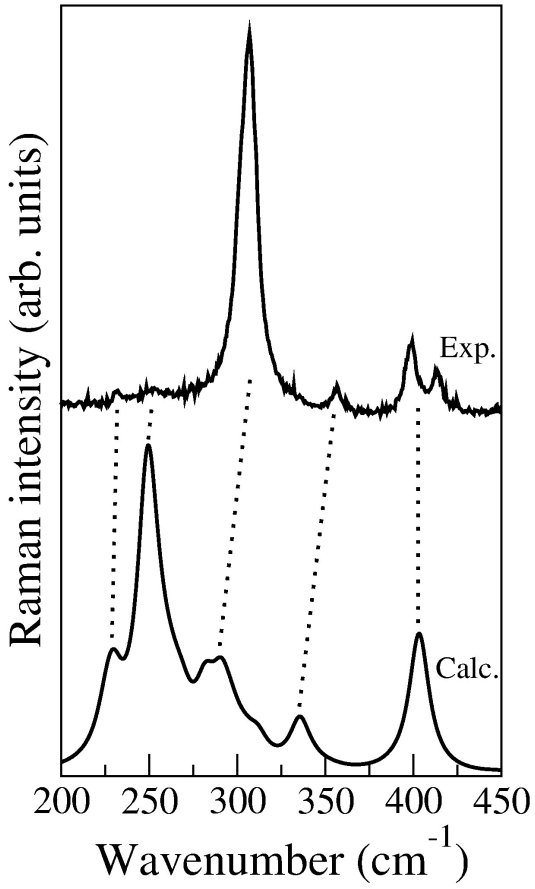

FIG. 7: Calculated (nonresonant) and experimental (using 633 nm laser line, resonant case) Raman spectrum of a $CrSi_2$ polycrystalline powder. We assume a Lorentzian line shape and a constant linewidth fixed at 7 cm^{-1} in the calculated spectrum.